

Perfect Absorption in Complex Scattering Systems with or without Hidden Symmetries

Lei Chen,^{1,2} Tsampikos Kottos,³ and Steven M. Anlage^{1,2}

¹*Quantum Materials Center, Department of Physics,
University of Maryland, College Park, MD 20742, USA*

²*Department of Electrical and Computer Engineering,
University of Maryland, College Park, MD 20742, USA*

³*Department of Physics, Wesleyan University, Middletown, CT 06459, USA*

(Dated: September 14, 2022)

Wavefront shaping (WFS) schemes for efficient energy deposition in weakly lossy targets is an ongoing challenge for many classical wave technologies relevant to next-generation telecommunications, long-range wireless power transfer, and electromagnetic warfare. In many circumstances these targets are embedded inside complicated enclosures, such as complex networks, buildings, or vessels, where the hypersensitive nature of chaotic scattering challenges the viability of WFS protocols. We demonstrate the success of a new and general WFS scheme, based on coherent perfect absorption (CPA) electromagnetic protocols, by utilizing a generic complex scattering system - a network of coupled transmission lines with complex connectivity. Our platform allows for control of the local losses inside the network and of the violation of time-reversal symmetry via a magnetic field. Our platform allows us to go beyond the initial concept of CPA as the time-reversal of a laser cavity and provides a more general framework where WFS in wave chaotic systems can be investigated using semiclassical tools, thus opening up CPA to much broader relevance in the real world.

Coherent perfect absorption (**CPA**) has been appealing to physicists and engineers for both its fundamental and technological relevance. On the technological level its implementation promises the realization of a novel family of wave-based devices performing highly-selective and tunable absorption in a manner that goes beyond the traditional concept of “impedance matching”. On the fundamental level, CPA has traditionally been associated with the concept of time-reversal symmetry, one of the most fundamental symmetries in nature. In its original conception CPA was proposed as the time-reversal of a laser cavity^{1,2}: Specifically, it is a lossy cavity that acts as a perfect interferometric trap for incident radiation, provided that its spatial distribution matches the one that would be emitted from the same cavity if the loss mechanism is substituted by a corresponding gain mechanism i.e. if the cavity turns into a laser. Practically speaking, the CPA process works by taking waves of particular amplitude and phase (coherent illumination)² from a number of input channels and causing them to interfere and to be completely absorbed by losses in the system. Remarkably, even an arbitrarily small amount of loss can be used to completely absorb the incident radiation if the system is sufficiently reverberant³. Nearly all early realizations of CPA have followed this basic paradigm and have utilized structures or coherent illumination conditions with very special symmetries. Here we experimentally demonstrate the concept of coherent perfect absorption in a new generalized setting where the lossy cavity is a generic complex scattering system having no special symmetries. We implement this scenario using a microwave graph constructed from coaxial cables connected by Tee-junctions. By adding a simple variable lossy attenuator into the system, we can clearly identify the CPA frequencies as the complex zeros of the scat-

tering matrix which cross the real frequency axis and achieve perfect absorption in this complex scattering setting. Most importantly, our experimental set-up allows us to demonstrate that the concept of CPA can be extended beyond the case where time-reversal (**TR**) symmetry holds. The latter can be achieved by introducing a circulator into the microwave graph⁴. Our experimental platform, due to its elegant simplicity, provides a convenient tool for the study of CPA in generic complex scattering systems having neither geometric nor dynamical symmetries. However, the results are extremely general and apply to all wave frameworks. Moreover, our approach paves the way for the analysis of CPA waveforms and frequencies in terms of semiclassical tools and trace formulae⁵⁻⁷, which can be used as design tools for optimizing CPA traps by utilizing their system-specific characteristics.

CPA phenomena have been theoretically proposed in a number of contributions^{1,8-14}, but only a few experimental works have reported a realization of a CPA in a variety of platforms and settings. At first it was demonstrated with free-space counter-propagating waves impinging on lossy slabs in the form of semiconductors², metasurfaces¹⁵, graphene-based structures¹⁶, Parity-Time (\mathcal{PT}) symmetric electronic circuits¹⁷ and \mathcal{PT} -symmetric quantum well waveguides that act as both a laser and CPA absorber¹⁸, and acoustic systems^{19,20}. Multi-port CPA was also achieved using a diffraction grating and lossy plasmonic modes (this work employed a pair of non-reciprocal scattering channels, but did not break time-reversal invariance)²¹. Most of these experimental demonstrations of CPA have generally been performed in open systems with freely counter-propagating waves arriving on a loss center at normal incidence. Such a configuration puts a strong constraint on the

loss required to achieve CPA (e.g. 50% single-beam absorption²²), and this is a significant limitation of such “free space optical” approaches. In summary, these early demonstrations used highly symmetric structures and excitation conditions to achieve CPA. Now the challenge is to considerably generalize the phenomenon and realize CPA in wave chaotic or disordered media without special geometrical or hidden symmetries. It is clear that the reverberations, complex interference, and losses present in wave- or quantum-chaotic systems constitute a challenge for achieving CPA. Recently a demonstration of CPA was achieved in a multiple scattering environment with many input and output channels, implementing effectively a random anti-laser²³. This demonstration, however, utilized the conventional anti-laser concept, and is limited to a mechanically-tunable loss element. It is desirable to expand the range of CPA to include complex and chaotic scattering environments of all kinds. Importantly, one has to investigate the applicability of CPA under controllable time-reversal symmetry violation conditions.

There are a number of deficiencies associated with the previous efforts to measure CPA. Some of these schemes failed to directly measure the outgoing waves from the system, but deduced the CPA condition by calculating the output signals based upon combinations of data (usually the scattering matrix) taken under other (non-CPA) conditions. Obviously, a CPA platform that will allow for a direct measurement of the output signal will open up new technological opportunities, as proposed in the photonic context³. Secondly, the degree to which the CPA condition is achieved has only been quantitatively demonstrated to a limited extent, typically 1 part in 10^2 , not at all close to the expected ideal outcome. Third, the previous experimental efforts have implemented loss in a way that is difficult to control and systematically vary, such as the thickness of a slab, or the temperature variation of conductivity. We introduce a convenient electronically-tuned loss center that permits continuous and precise control of nearly ideal CPA conditions. Needless to say, the reconfigurability feature that is provided by our platform is highly desirable in actual photonics applications. Finally, all previous works have been limited to systems that display time-reversal invariance (**TRI**) for the wave propagation (beyond the trivial **TRI**-breaking effects of dissipation). In our experiment we explicitly demonstrate CPA in a non-reciprocal broken-**TRI** system, greatly expanding the impact and utility of the CPA phenomenon. Such analysis proves that the concept of CPA goes far beyond its initial conception as a “time-reversed laser”.

Complex over-moded networks have proven to be a simple, yet powerful platform where wave phenomena of systems with underlying classical chaotic dynamics can be experimentally demonstrated and theoretically analyzed using semiclassical tools^{24,25}. Complex scattering systems show extreme sensitivity to boundary conditions, a property that is inherited from the underlying chaotic ray dynamics in the classical limit. These systems display

universal statistical properties hypothesized to be described by random matrix theory²⁶. However, most practical systems also show deviations from universal chaotic behavior due to short orbits²⁷, mixed chaotic and regular phase space²⁸ (perhaps arising from parallel walls), inhomogeneous loss, etc. Thus our platform, being a generic complex scattering system, demonstrating both the extreme sensitivity to perturbations and typical deviations from universal statistical behavior²⁹, is an ideal surrogate for real-world scattering systems. Complex wave networks have been used to model mesoscopic quantum transport³⁰, sound and electromagnetic energy propagation through multiply-connected arrays of compartments, and chains of coupled electromagnetic cavities³¹.

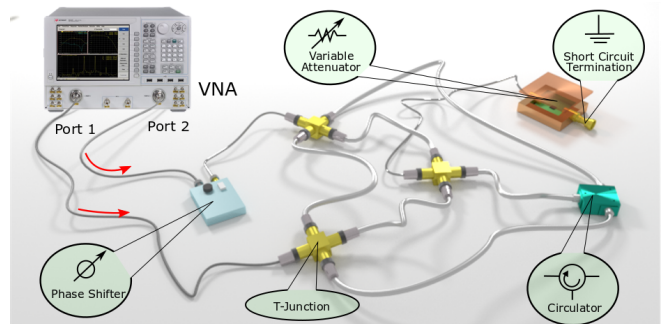


FIG. 1. Experimental setup of the CPA state measurement. A PNA-X (network analyzer with two internal sources) is used to generate microwaves with well-defined frequency and relative amplitudes at the two ports as the CPA state excitation signals. Coherent phase control between the two excitation signals is realized by placing a phase shifter between port 2 of the network analyzer and the graph. The outgoing and returning waves are directly measured by the PNA-X. On the right side of the figure is the tetrahedral microwave graph formed by coaxial cables and Tee-junctions. The four-way adapter shown in the figure is realized by connecting two Tee-junctions together in the real experiment. One node of the graph is loaded with a variable attenuator to provide parametric variation of the scattering system. One other node is made from either a Tee-junction (**TRI**) or a 3-port circulator (**BTRI**) to create a **TRI** system or a broken-**TRI** system, respectfully.

Our experiment utilizes a tetrahedral microwave graph formed by coaxial cables and Tee-junctions^{32,33}. A variable attenuator is attached to one internal node of the graph (see Fig. 1). The system is coupled to external transmission lines attached to N specific nodes of the graph. Each coupling transmission line (labelled with a red arrow in Fig. 1) is a coaxial cable supporting a single propagating mode connecting to one port of the Vector Network Analyzer (VNA). The plane of calibration of the VNA is at the point where the transmission line attaches to the port of the graph. The experimental setup is completed with the addition of a phase shifter. The latter will be used in the second part of our experiments when we will launch the appropriate CPA waveforms into the complex network (see below).

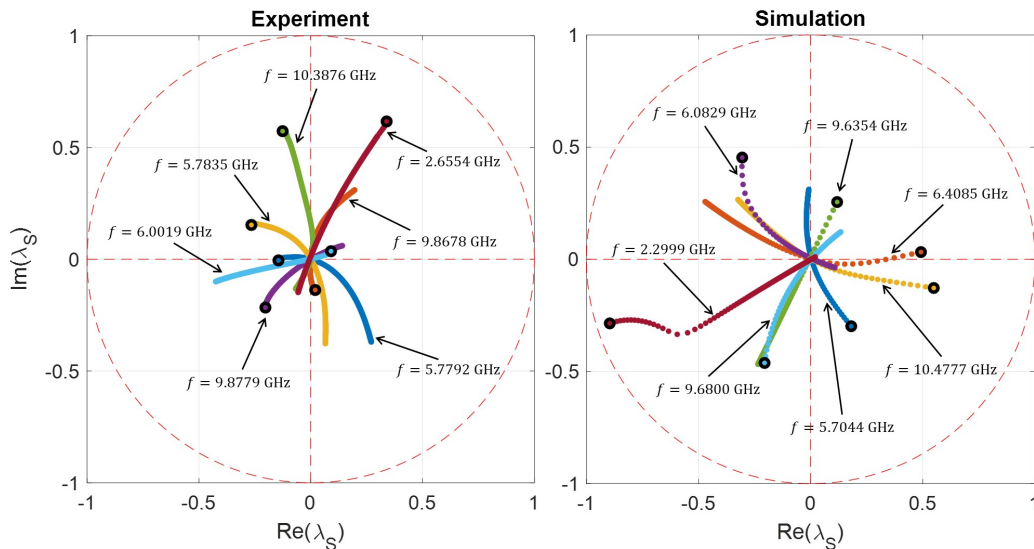


FIG. 2. Plot of selected S-matrix eigenvalues as a function of attenuator setting in the tetrahedral graph showing examples of near-zero-crossing trajectories. Selected eigenvalues of the S-matrix are plotted in the complex λ_S plane, where the red dashed circle represents the unit circle. The left figure shows experimental data, while the right figure shows data from the simulation. Each trajectory represents one frequency (color coded), and the corresponding frequency for each trace is labelled in the figure. The black circle at the start of every trajectory indicates the initial eigenvalue at minimum attenuation, and as attenuation increases, the eigenvalue goes nearly through the origin in the complex plane.

The wave transport properties of such a system are succinctly summarized by the $N \times N$ complex scattering matrix S . The S-matrix connects the incoming and outgoing waves through these N channels as $\phi_{out} = S\phi_{in}$, where ϕ_{out} (ϕ_{in}) is an N -component vector of outgoing (incoming) wave amplitudes and phases that defines the scattered outgoing (incoming) field in the channel-mode space. In the case of coherent perfect absorption all input energy is absorbed by the system, thus requiring ϕ_{out} to be zero. This physical condition is mathematically formulated by the requirement that $S\phi_{in} = 0$ for non-zero ϕ_{in} . The latter condition is equivalent to the requirement that the S-matrix is not invertible i.e. it has a zero eigenvalue $\lambda_S = 0$. The associated eigenvector provides the incident waveform configuration that leads to a CPA. Note that this requirement does not violate any constraints of the S-matrix, which in the case of CPAs is sub-unitary due to the presence of an absorbing center inside the scattering domain. Let us finally point out that the eigenvalues of the S-matrix are functions of the frequency ω of the incident waveform i.e. $\lambda_S = \lambda_S(\omega)$. From the mathematical perspective, one cannot exclude the possibility to have complex ω 's as roots of the CPA condition $\lambda_S(\omega) = 0$. These complex zeros, however, are unphysical since they do not correspond to incident propagating plane waves and therefore have to be excluded from the set of acceptable CPA solutions. Of course, the reality of ω is not an issue in the experimental analysis since the measured S-matrix is always evaluated at real frequencies.

By solving for the eigenvalues of the measured S-

matrix, the CPA condition can be found, in principle. However it is very unlikely to find a true zero of the complex eigenvalues at a given energy of the incident waves and system configuration. Thus one must utilize the parametric dependence of the S-matrix on the internal dissipation strength to establish the zero eigenvalue condition. In this setup we exploit the energy (wavelength) and lossyness (attenuation) of a complex scattering system as two parameters, and this provides enough freedom to find true S-matrix zeros. Once the CPA condition is found, the required system loss configuration and stimulus energy are known, and the corresponding S-matrix eigenvector specifies the incoming stimulus wave amplitudes and phases (i.e. coherent excitation). When this eigenvector is applied as the input excitation, there should be zero outgoing wave energy from all N of the scattering channels of the system. It should be noted that this procedure is entirely general and doesn't depend on the nature of the wave phenomenon or on the presence or absence of chaotic scattering in the system.

Results. Following this approach, the 2×2 scattering matrix of the graph can be acquired using the setup of Fig. 1 (excluding the phase shifter). The measurement is taken from 10 MHz to 18 GHz which includes about 420 modes of the closed graph. The calibrated S-matrix of the 2-port graph is then measured under different attenuation settings ranging from 2 dB to 12 dB (which includes the insertion loss of the variable attenuator). Implementing a matrix diagonalization technique, the complex eigenvalues λ_S of the S-matrix are found for each frequency and attenuator setting. A limited num-

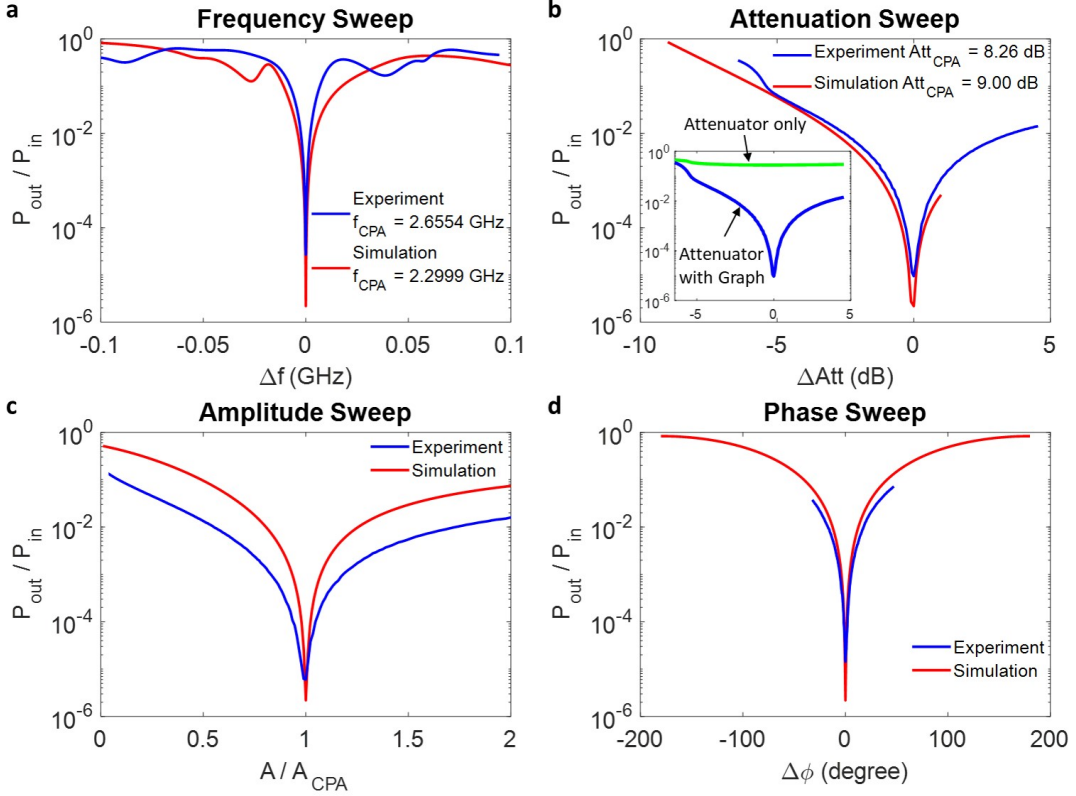


FIG. 3. **Evidence of CPA in the complex network under four independent parametric sweeps.** Plots are normalized so that CPA conditions are in the center of the parameter variation range. The closest frequency CPA condition for the simulation is plotted along with the experimental data. **a** | Measured ratio of output power P_{out} to input power P_{in} as the microwave frequency sent into both ports of the graph is simultaneously swept near the CPA frequency ($\Delta f = f - f_{CPA}$). The output-to-input power ratio shows a sharp dip below 10^{-4} at the CPA frequency (f_{CPA}) in both experiment and simulation. **b** | Output to input power ratio obtained by varying the attenuation of the variable attenuator in the graph. ΔAtt is the attenuation normalized by Att_{CPA} from the CPA condition. Inset shows the absorption difference between the attenuator only and the attenuator embedded in the graph. **c,d** | Output to input power ratio obtained by changing the amplitude A (**c**) and phase difference $\Delta\phi$ (**d**) separately of the two excitation signals required for the CPA state. The absorption of power reaches its maximum at the CPA configuration, and quickly deteriorates for even small offset from the CPA condition. All experimental results are obtained by direct measurement of the input and output RF powers.

ber of these eigenvalues will approach the origin in the complex λ_S plane (see Fig. 2). These near-zero crossings are then examined in detail. Through this method, the specific frequencies and attenuation values at the “zero-crossing” CPA state, as well as the required excitation relative magnitude and phase at the two ports (S-matrix eigenvector) are then determined.

Using the information obtained from the S-matrix measurement, the CPA conditions are identified, and we can directly test them experimentally. To do this, a two-source VNA is used to apply signals at the CPA frequency but with two different amplitudes (see Fig. 1). In addition, a phase shifter is added between port 2 of the network analyzer and the graph in order to deliver signals with the appropriate phase difference to the two ports of the graph. When signals are sent from both ports of the network analyzer simultaneously, it should be possible to observe the coherent perfect absorption, namely no mi-

crowave signals should emerge from the graph through either of the ports. The VNA measures both the outgoing and incoming waves at the plane of calibration, hence the CPA condition can be directly confirmed with this setup.

Under the CPA condition, a nearly perfect absorption is achieved, and it has been verified using four independent parametric sweep measurements (see Fig. 3). Both experimental and numerical data are plotted in the same figure. Parameters swept include the microwave frequency (wavelength), attenuation of the variable attenuator embedded in the graph, amplitude of excitation signal at port 1, and phase of excitation signal at port 2, while keeping other settings unchanged at the CPA condition. The input wave power and outgoing wave power are directly measured while changing the system configuration or the input stimulus setting. The ratio of outgoing signal power over input signal power (P_{out}/P_{in}) acquires

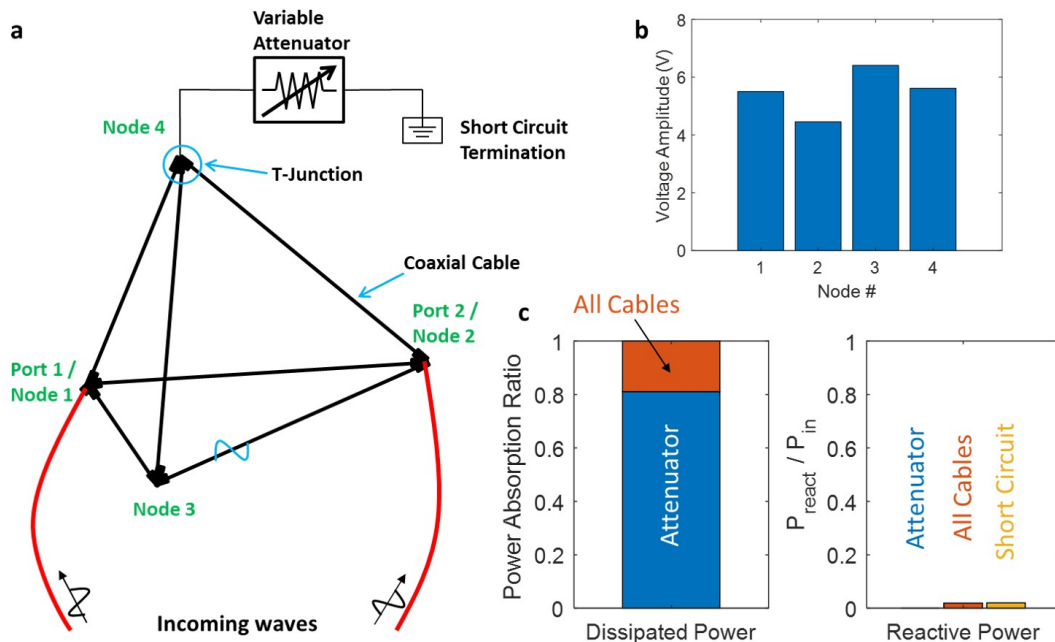


FIG. 4. **Voltage profile and power distribution of CPA state in simulation.** **a** | Schematic of the microwave graph with labelled ports under CPA condition at 2.2999 GHz in simulation. **b** | Voltage profiles of four nodes in the graph under CPA condition. **c** | Power distribution among the graph components under the CPA condition. Left plot shows that about 80% of the power are being dissipated on the attenuator, while the remainder is dissipated on the cables. Right plot shows reactive power on the cables and short circuit. Compare with the “Anti-CPA” condition in Fig. S2 in the Supplementary Information.

values as low as 10^{-5} at the CPA condition, and both experiment and simulation show similar behavior upon deviation from the CPA conditions. Figure 3 demonstrates that the minimum outgoing power is measured at precisely the CPA condition, and rapidly increases in a cusp-like manner as any of the parameters deviate from that condition.

Due to the extreme sensitivity to perturbations and internal system details, it is naturally difficult to create a numerical model of a complex scattering system that reproduces all of its properties in detail. Instead, the numerical results in Figs. 2, 3 and 5 are taken from a simplified model that approximates the measured graph but captures the essential properties of all complex scattering systems. The model demonstrates that the CPA results are *generic* to complex scattering systems, establishing the breadth and generality of our results.

To emphasize the importance of having a reverberant cavity instead of a “bare” attenuator only, we measure the power ratio of the “bare” attenuator (see Fig. 3b inset) under the same settings as in the complex networks. From the inset, we can see that in the absence of the graph, the attenuator can only absorb a small fraction of the incident power ($P_{out}/P_{in} > 10^{-1}$). This illustrates the importance of having the complex network as the “cavity” to create the CPA condition.

Both the variable attenuator and the microwave graph “cavity” play important roles in the coherent perfect absorption of the incident power. Here we investigate the

contribution to the total power absorption from different elements in this setup, as well as the reverberation effect inside the graph under CPA condition using the simulation model shown in Fig. 4a (for further details see the Supplementary Information). Fig. 4b shows that the voltage amplitudes at the four nodes in the graph under CPA condition are roughly equal. As shown in Fig. 4c, most of the power is absorbed by the variable attenuator, and the rest is absorbed by the coaxial cables, which contribute to a spatially-uniform absorption inside the system. There is very little reactive power in the graph under the CPA condition, as opposed to the “Anti-CPA” state where a large amount of reactive power circulates in the system (see Fig. S2c in the Supplementary Information). Therefore, Figure 4 exactly demonstrates what the theory predicts: the coherent perfect absorption is the combined effect of localized loss and intricate wave interferences, providing a perfect destructive interferometric trap for the incident radiation.

After exploring the coherent perfect absorption property of the TRI tetrahedral microwave graph, a graph with BTRI (Broken-Time Reversal Invariance) was realized. CPA associated with violated time-reversal symmetry is novel, and is completely different from its original definition^{1,2}, challenging the idea that CPA is simply a time-reversed laser. Driven by such motivation, we added a circulator⁴ at one internal node of the tetrahedral graph (see Fig. 1), and turned a TRI graph into a BTRI graph. Previous work demonstrated that the statistics of the mi-

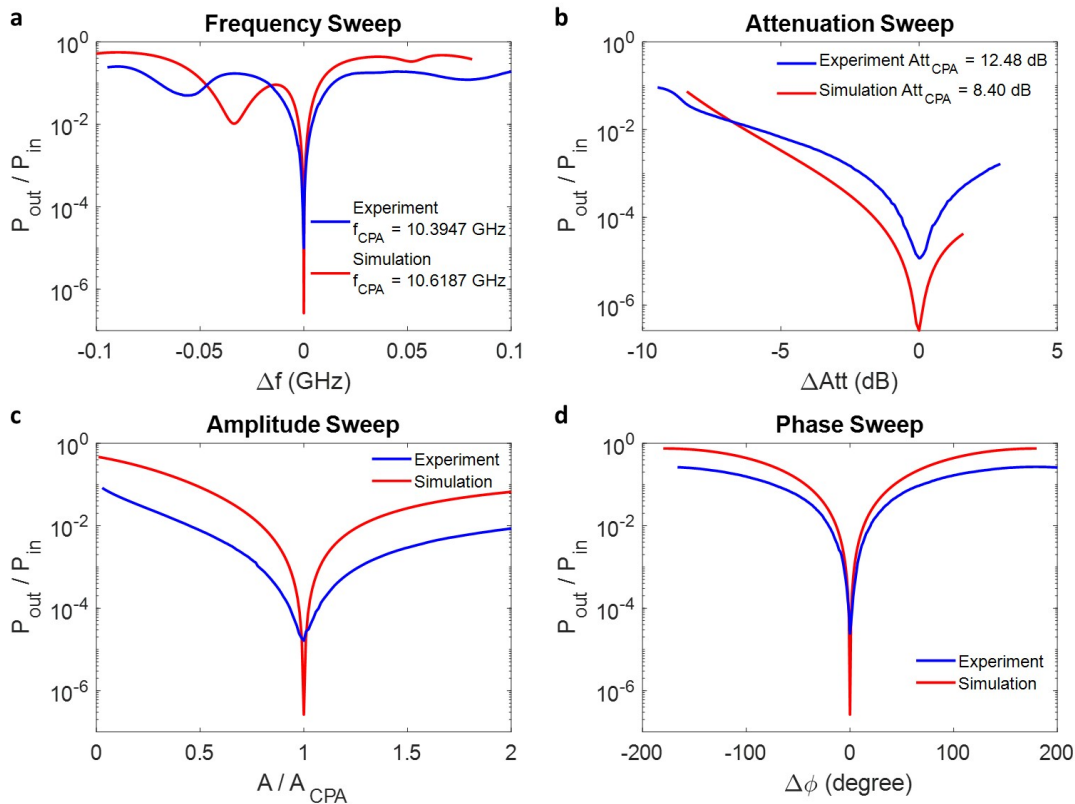


FIG. 5. **Evidence of CPA in the complex network with BTRI under four independent parametric sweeps.** Plots are normalized so that CPA conditions are in the center of the parameter variation range. The closest CPA frequency condition for the simulation is plotted along with the experimental data. **a** | Measured ratio of output power P_{out} to input power P_{in} as the microwave frequency sent into both ports of the graph is simultaneously swept near the CPA frequency ($\Delta f = f - f_{CPA}$). The output-to-input power ratio shows a sharp dip below 10^{-4} at the CPA frequency (f_{CPA}) in both experiment and simulation. **b** | Output to input power ratio obtained by varying the attenuation of the variable attenuator in the graph. ΔAtt is the attenuation normalized by Att_{CPA} from the CPA condition. **c,d** | Output to input power ratio obtained by changing the amplitude A (**c**) and phase difference $\Delta\phi$ (**d**) separately of the two excitation signals required for the CPA state. All experimental results are obtained by direct measurement of the input and output RF powers.

crowave graph impedance (or reaction matrix) changed from that characterized by the Gaussian orthogonal ensemble of random matrices (appropriate for TRI systems) to the Gaussian unitary ensemble (appropriate for BTRI systems) with the addition of this circulator^{34,35}.

Following the same procedure as for the TRI graph experiment, the CPA conditions are found by solving for the eigenvalues of the S-matrix. After that, similar sweep measurements are done as in the TRI case to directly verify the coherent perfect absorption in the BTRI graph. The results in Fig. 5 from both experiment and simulation show similar CPA behavior as observed in the TRI case, which serves to generalize CPA to BTRI settings as well. Naively, by introducing the non-reciprocal element (circulator) into the system, one would expect that the broken-TRI should weaken the coherence between incident waves, as seen in the eigenfunctions of BTRI wave chaotic systems³⁶. Yet the results shown here demonstrate the applicability of CPA theory even to BTRI systems.

The implementation of CPA in generic complex scattering systems opens up a number of new applications. The first is long-range wireless electromagnetic power transfer technologies that seek to deliver significant electromagnetic power to a single designated object located inside a complex scattering enclosure many wavelengths away from the source. Current approaches utilize multiple scattering and interfering wave trajectories connecting power source and target through either time-reversal³⁷ or phase conjugation of microwave signals³⁸ that involve either large bandwidth or a large numbers of channels. These methods suffer from low efficiency as well as radiation safety concerns. A CPA-based method would require only that the target employs a tunable loss, or other tunable scattering property³⁹⁻⁴¹, and that the source employs only a small number of channels to measure the S-matrix of the enclosure to find the CPA condition. Once CPA is established, the source would output a coherent energetic signal that would be maximally absorbed at the desired target, with minimal loss elsewhere

in the environment. As an added benefit other users can utilize the same bandwidth to perform other tasks (e.g. information transfer) utilizing the “Anti-CPA” condition (see the Supplementary Section 2), alleviating frequency crowding concerns. A second application concerns sensing of minute changes in a scattering environment. There will be a sensitive change in absorbed energy, or output power from a complex scattering structure, due to any perturbation of the system from CPA condition, as illustrated by the cusp-like features in Figs. 3 and 5. This arises from the dramatic shift of the scattering matrix zero off of the real-frequency-axis, and is a very direct and easy to measure property. This sensing protocol is simpler than the frequency splitting of degenerate modes created by a perturbation to an optical resonator tuned to an exceptional point⁴², for example. Our CPA approach, which relies in the natural complexity of the cavity, is generic and will work in any wavelength regime (or for any wave phenomenon) as long as it is performed in a complex scattering environment. A third example application is a new CPA protocol for secure communications. Consider that the absorber is a target receiver embedded at an unknown location in a complex environment. Due to the complexity of the environment (sensitive interference), transfer of information from an outside source occurs only if the emitter prepares and injects a very specific waveform. The waveform has to be determined by the absorber property as well as the environment information, and is rapidly altered as soon as the absorber changes its property. The CPA conditions (absorption and frequency) could be utilized to create a unique “key” to encrypt the communication and secure the transmission process. Through this method one can establish a secure communication protocol between the emitter and the absorber.

In summary we demonstrate the first coherent perfect absorption in a generic complex scattering system, namely a microwave realization of a quantum graph. The CPA condition is realized through continuous tuning of a lossy component and by means of direct measurement of RF power coming out of the graph. As much as 99.999% of the injected power are absorbed by the system. We also demonstrate the first CPA implementation in a system with broken-time reversal invariance, which opens a much broader domain for CPA application. Our work demonstrates that CPA can indeed be achieved even in the case of complex (or chaotic) scattering set-ups where small variations in the form of the incoming waves or of the scattering system might lead to dramatic changes in the scattering fields. The results are independent of the presence or absence of chaos in the classical limit and hold for any real-world complex scattering system and any wave phenomenon. This work generalizes the operations and settings for CPA and is expected to motivate practical applications, including designing extremely efficient absorbers, enabling practical long-range wireless power transfer, and associated high-efficiency energy conversion systems. The extreme sensitivity of absorption to para-

metric variation away from the CPA condition can be utilized for ultra-sensitive detectors and secure communication links. These ideas translate to all forms of complex wave scattering, including audio acoustics and solid-body vibro-acoustics. For future work, the chaotic CPA phenomenon can be extended to the nonlinear regime⁴³ by introducing nonlinear elements into the system.

METHODS

Experimental setup. Our experimental setup is a tetrahedral microwave graph constructed from six coaxial cables connected by coaxial Tee-junctions. The cables are semi-flexible SF-141 coaxial cables, each of different length, with SMA male connectors on both ends (Model SCA49141) obtained from Fairview Microwave, Inc.. The dielectric material of the cable is solid polytetrafluoroethylene (PTFE), which has a relative dielectric constant of 2.1. The inner conductor of the cable is silver plated copper clad steel (SPCW), and has a diameter of 0.036 inch (0.92 mm); while the outer shield is a copper-tin composite which has an inner diameter of 0.117 inch (2.98 mm). The dielectric loss tangent of the medium is $\tan\delta = 0.00028$ at 3 GHz, and the resistivity of the metals in the cable is $\rho = 4.4 \times 10^{-8} \Omega \cdot m$ at 20 °C. The lengths of the six cables are 13, 14, 15, 16, 18 and 20 inch. The total length of the graph is then approximately 2.44 m, giving rise to a mean spacing between modes of 42.4 MHz, which is constant as a function of frequency. On one node of the graph, two Tee-junctions form a four-way adapter where a voltage variable attenuator (HMC346ALC3B from Analog Devices, Inc.) is connected to one connector. A short circuit termination is connected to the other end of the attenuator. Using a Keithley power supply (2231A-30-3), the attenuation of the variable attenuator is continuously swept by varying the supplied voltage from 4.00 V to 7.00 V. To find the appropriate CPA condition of the setup, we perform the S-matrix measurement of the graph in the frequency range from 10 MHz to 18.01 GHz (at 96,001 equidistant frequency points) which includes about 420 modes of the closed graph, with varying attenuation from about 2 dB to 12 dB (which includes the insertion loss of the variable attenuator). The attenuation is swept with a step size of roughly 0.1 dB. In the case of a BTRI microwave graph, a ferrite circulator (Model 4925 from Narda-MITEQ) is added to one node of the graph (see Fig. 1). The circulator has an operational frequency range from 7 GHz to 12.4 GHz, which constrains the frequency range of measurement accordingly. By connecting the microwave graph to a two-port VNA, with a coupling strength of about 0.68, we can obtain the S-matrix of the system under different attenuation configurations.

Verification of the CPA state. In order to create the coherent stimulus signals, we use a two-source VNA (PNA-X N5242A from Agilent Technologies, Inc.) to serve as the RF signal source and measure the incom-

ing and outgoing wave energies as well. The PNA-X has two built-in RF sources which provides great convenience for us to individually adjust the amplitudes of the two input excitation signals. The relative phase difference of the two input signals is controlled by adding a manual coaxial phase shifter between the VNA and port 2 of the graph (see Fig. 1). With this measurement setup, we can effectively tune the input stimulus signals for the CPA state as well as the system configurations, perform comprehensive parametric sweep measurements (see Fig. 3 and Fig. 5), and directly measure the input power P_{in} and output power P_{out} of the graph.

Simulation model. To compare with the experimental results and better understand the power distribution inside the system under CPA conditions, we set up a comparable simulation model in CST (Computer Simulation Technology) Studio. CST is commercial software specifically designed for electromagnetic field simulation, and we use the Circuits & Systems module to simulate the microwave graph. Coaxial cables are simulated by the preset simulation block in the software - coaxial lines, and the characteristic properties are mimicked by setting the corresponding parameters from the product datasheet. There are two loss mechanisms in the cable model: one is the dielectric loss tangent of the medium, and the other one is the metal resistivity. Both values are obtained from the cable datasheet, and the cable lengths are set exactly to model the real experiment. The Tee-junctions are set to be ideal for computational simplicity, and the attenuator is set to have continuously variable attenuation for the purpose of parameter sweep simulation. The coupling strength between the graph and the source ports is around 0.58 in the simulation, similar to that in the experiment. In the case of BTRI, an ideal circulator is added to one node of the graph corresponding to the experimental setup, and its scattering matrix is

$$S = \begin{pmatrix} 0 & 0 & 1 \\ 1 & 0 & 0 \\ 0 & 1 & 0 \end{pmatrix}$$

Therefore, following the same procedure as in the experiment, we can verify the CPA phenomena in the simulation as well.

ACKNOWLEDGEMENTS

This work is supported by the AFOSR under COE Grant FA9550-15-10171, the ONR under Grants N000141912481 and N00014-19-1-2480, and the Maryland Quantum Materials Center. We acknowledge S. Suwunnarat for helping us with the drawing of Fig. 1.

AUTHOR CONTRIBUTIONS

L. C. conducted the measurements and carried out the simulation under the supervision of S. M. A.. L. C. performed the data analysis under the guidance of T. K. and S. M. A.. L. C. wrote the manuscript with input from all co-authors.

COMPETING INTERESTS

The authors declare no competing interests.

MATERIALS AND CORRESPONDENCE

Correspondence and requests for materials should be addressed to L. Chen (email: lchen95@umd.edu) and S. M. Anlage (anlage@umd.edu).

DATA AVAILABILITY

The data that support results presented in this paper and other findings of this study are available from the corresponding authors upon reasonable request.

-
- [1] Y. D. Chong, L. Ge, H. Cao, and A. D. Stone, *Physical Review Letters* **105**, 053901 (2010).
- [2] W. Wan, Y. Chong, L. Ge, H. Noh, A. D. Stone, and H. Cao, *Science* **331**, 889 (2011).
- [3] D. G. Baranov, A. Krasnok, T. Shegai, A. Alù, and Y. Chong, *Nature Reviews Materials* **2**, 17064 (2017).
- [4] M. Ławniczak, S. Bauch, O. Hul, and L. Sirko, *Physical Review E* **81**, 046204 (2010).
- [5] J. Kuipers, D. V. Savin, and M. Sieber, *New Journal of Physics* **16**, 123018 (2014).
- [6] S. Muller and M. Sieber, in *The Oxford Handbook of Random Matrix Theory* (Oxford: Oxford University Press, 2011) edited by G. Akemann, J. Baik, and P. Di Francesco.
- [7] K. Richter and M. Sieber, *Physical Review Letters* **89**, 206801 (2002).
- [8] S. Dutta-Gupta, O. J. F. Martin, S. Dutta Gupta, and G. S. Agarwal, *Optics Express* **20**, 1330 (2012).
- [9] S. Dutta-Gupta, R. Deshmukh, A. Venu Gopal, O. J. F. Martin, and S. Dutta Gupta, *Optics Letters* **37**, 4452 (2012).
- [10] M. Kang, F. Liu, T.-F. Li, Q.-H. Guo, J. Li, and J. Chen, *Optics Letters* **38**, 3086 (2013).
- [11] J. Zhang, C. Guo, K. Liu, Z. Zhu, W. Ye, X. Yuan, and S. Qin, *Optics Express* **22**, 12524 (2014).
- [12] W. Zhu, F. Xiao, M. Kang, and M. Premaratne, *Applied Physics Letters* **108**, 121901 (2016).
- [13] H. Li, S. Suwunnarat, R. Fleischmann, H. Schanz, and T. Kottos, *Physical Review Letters* **118**, 044101 (2017).

- [14] Y. V. Fyodorov, S. Suwunnarat, and T. Kottos, *Journal of Physics A: Mathematical and Theoretical* **50**, 30LT01 (2017).
- [15] J. Zhang, K. F. MacDonald, and N. I. Zheludev, *Light: Science & Applications* **1**, e18 (2012).
- [16] S. M. Rao, J. J. F. Heitz, T. Roger, N. Westerberg, and D. Faccio, *Optics Letters* **39**, 5345 (2014).
- [17] J. Schindler, Z. Lin, J. Lee, H. Ramezani, F. M. Ellis, and T. Kottos, *Journal of Physics A: Mathematical and Theoretical* **45**, 444029 (2012).
- [18] Z. J. Wong, Y. L. Xu, J. Kim, K. O'Brien, Y. Wang, L. Feng, and X. Zhang, *Nature Photonics* **10**, 796 (2016).
- [19] C. Meng, X. Zhang, S. T. Tang, M. Yang, and Z. Yang, *Scientific Reports* **7**, 43574 (2017).
- [20] M. Lanoy, R.-M. Guillermic, A. Strybulevych, and J. H. Page, *Applied Physics Letters* **113**, 171907 (2018).
- [21] J. W. Yoon, G. M. Koh, S. H. Song, and R. Magnusson, *Physical Review Letters* **109**, 257402 (2012).
- [22] S. Li, J. Luo, S. Anwar, S. Li, W. Lu, Z. H. Hang, Y. Lai, B. Hou, M. Shen, and C. Wang, *Physical Review B* **91**, 220301 (2015).
- [23] K. Pichler, M. Kühmayer, J. Böhm, A. Brandstötter, P. Ambichl, U. Kuhl, and S. Rotter, *Nature* **567**, 351 (2019).
- [24] T. Kottos and U. Smilansky, *Physical Review Letters* **79**, 4794 (1997).
- [25] S. Gnutzmann and U. Smilansky, *Advances in Physics* **55**, 527 (2006).
- [26] O. Bohigas, M. J. Giannoni, and C. Schmit, *Physical Review Letters* **52**, 1 (1984); G. Casati, F. Valz-Gris, and I. Guarneri, *Lettere al Nuovo Cimento* **28**, 279 (1980).
- [27] J. A. Hart, T. M. Antonsen, and E. Ott, *Physical Review E* **80**, 041109 (2009).
- [28] B. Dietz, T. Friedrich, M. Miski-Oglu, A. Richter, and F. Schäfer, *Physical Review E* **75**, 035203 (2007).
- [29] B. Dietz, V. Yunko, M. Białous, S. Bauch, M. Ławniczak, and L. Sirko, *Physical Review E* **95**, 052202 (2017).
- [30] D. Kowal, U. Sivan, O. Entin-Wohlman, and Y. Imry, *Physical Review B* **42**, 9009 (1990).
- [31] S. Ma, B. Xiao, Z. Drikas, B. Addissie, R. Hong, T. M. Antonsen, E. Ott, and S. M. Anlage, *Physical Review E* **101**, 022201 (2020).
- [32] O. Hul, O. Tymoshchuk, S. Bauch, P. M. Koch, and L. Sirko, *Journal of Physics A: Mathematical and General* **38**, 10489 (2005).
- [33] Z. Fu, T. Koch, T. M. Antonsen, E. Ott, and S. M. Anlage, *Acta Physica Polonica A* **132**, 1655 (2017).
- [34] Z. Fu, *A Wave Chaotic Study of Quantum Graphs with Microwave Networks*, Master's thesis, University of Maryland (2017), available at <http://hdl.handle.net/1903/20040>.
- [35] M. Ławniczak and L. Sirko, *Scientific Reports* **9**, 5630 (2019).
- [36] D. H. Wu, J. S. A. Bridgewater, A. Gokirmak, and S. M. Anlage, *Physical Review Letters* **81**, 2890 (1998).
- [37] F. Cangialosi, T. Grover, P. Healey, T. Furman, A. Simon, and S. M. Anlage, in *2016 IEEE Wireless Power Transfer Conference (WPTC)* (IEEE, 2016) pp. 1–4; R. Ibrahim, D. Voyer, A. Breard, J. Huillery, C. Voltaire, B. Allard, and Y. Zaatar, *IEEE Transactions on Microwave Theory and Techniques* **64**, 2159 (2016).
- [38] H. Zeine, "Wireless power transmission system," (2020), US Patent 10,566,846.
- [39] Y. V. Fyodorov and H.-J. Sommers, *Physical Review Letters* **76**, 4709 (1996).
- [40] P. Šeba, K. Życzkowski, and J. Zakrzewski, *Physical Review E* **54**, 2438 (1996).
- [41] A. Krasnok, D. G. Baranov, A. Generalov, S. Li, and A. Alù, *Physical Review Letters* **120**, 143901 (2018).
- [42] W. Chen, Ş. K. Özdemir, G. Zhao, J. Wiersig, and L. Yang, *Nature* **548**, 192 (2017).
- [43] A. Müllers, B. Santra, C. Baals, J. Jiang, J. Benary, R. Labouvie, D. A. Zezyulin, V. V. Konotop, and H. Ott, *Science Advances* **4**, eaat6539 (2018).

SUPPLEMENTARY INFORMATION

Supplementary section 1 - Experimental setup for S-matrix measurement

The S-matrix measurement involves the VNA and the microwave graph (see Fig. S1). Calibration is done at the end of two test cables (see red lines in Fig. S1) where they are connected to the graph. The S-matrix of the experimental setup is measured under many settings of the variable attenuator.

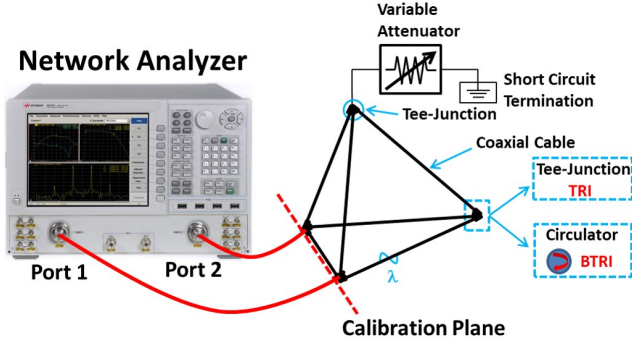


FIG. S1. **Schematic experimental setup of the S-matrix measurement.** The tetrahedral graph is formed by coaxial cables connected with Tee-junctions. One node of the graph is loaded with a voltage variable attenuator to provide parametric variation of the scattering system. One other node (blue dashed box) is made from either a Tee-junction (TRI) or a 3-port circulator (BTRI) to create a TRI system or a broken-TRI system, respectively.

Supplementary section 2 - Simulation of the “Anti-CPA” state

We introduce a new operator - the Absorption matrix $A \equiv \mathbb{1} - S^\dagger S$ to analyze the “Anti-CPA” state¹³. We point out that A is a Hermitian, positive semi-definite operator. The magnitude of its eigenvalues α span the interval $[0,1]$ and the corresponding eigenvectors $|\alpha\rangle$ are orthogonal. It is easy to show that the eigenvector associated with the eigenvalue $\alpha_{max} = 1$ is the CPA waveform that we have identified previously from the analysis of the zeroes of the S-matrix. It follows that the components of the eigenvector which is associated with the minimum eigenvalue α_{min} provides the shape of the incident waveform which will lead to *minimal* absorption. We refer to such a scattering field as the “Anti-CPA” state. The extreme case of $\alpha = 0$ is associated with a scattering field that avoids completely the vertex where the attenuator is located. We verify this effect by observing the voltage profile and energy distribution in the system under “Anti-CPA” stimulus at the same frequency in the simulation (see Fig. S2a). In Fig. S2b, the voltage on each node is much smaller than the voltage at CPA state (compare with Fig. 4b), and the voltage on node 4 where the attenuator is attached is particularly small. Under this condition, the total power absorption ratio is only 0.13, and nearly no power is absorbed by the attenuator (Fig. S2c), which characterizes the “Anti-CPA” state. Nevertheless, there is a great deal of reactive power present in the system (compare with Fig. 4c).

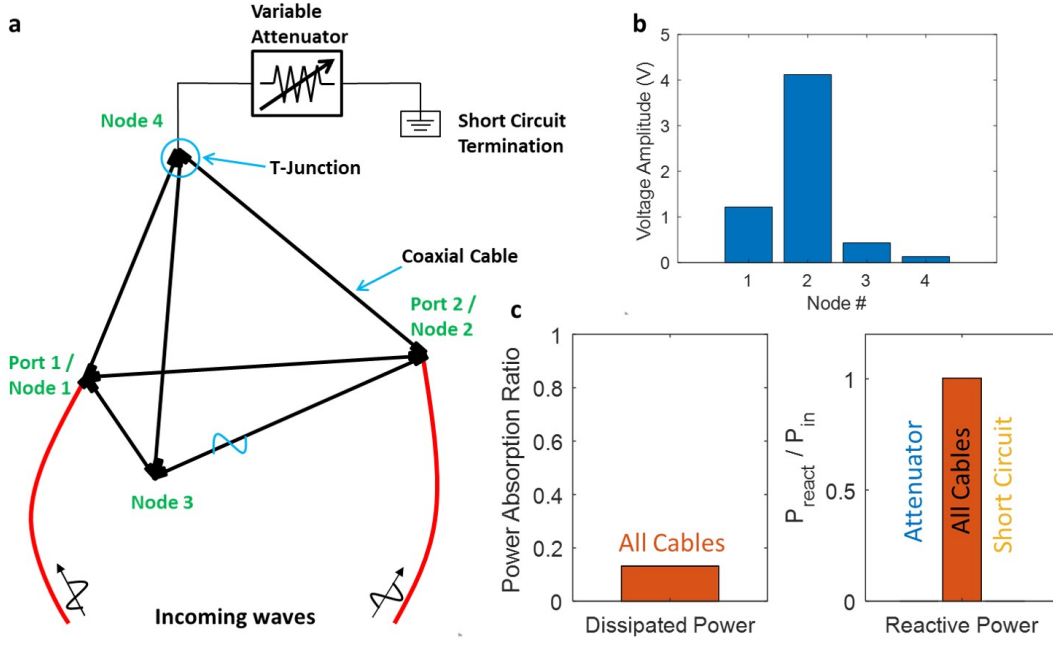


FIG. S2. **Voltage profile and power distribution of the “Anti-CPA” state in simulation.** **a** | Schematic of the microwave graph with labelled ports under CPA condition at 2.2999 GHz in simulation. **b** | Voltage profiles of four nodes in the graph under the “Anti-CPA” condition. The voltage amplitude on Node 4, where the absorbing attenuator is attached, is much less than the voltage amplitude on other nodes. **c** | Power distribution among the graph components under the “Anti-CPA” condition. Left plot shows that very little power (less than 15%) are absorbed by the graph components, and almost no power is dissipated by the attenuator. Right plot shows reactive power on the cables.